Observations of the Vortex Ring State

R.B. Green, E.A. Gillies, M. Giuni, J. Hislop
University of Glasgow
UK
and
Ö. Savaş
University of California at Berkeley
U.S.A.

Abstract

This paper considers the vortex ring state, a flow condition usually associated with the descent of a rotor into its own wake. The phenomenon is investigated through experiments on simple rotor systems, and a comparison is then made with observations of a flow generated by a specially designed open core, annular jet that generates a mean flow velocity profile similar to the mean flow in a rotor wake in hover. In an experimentally simulated descent, the jet flow generates a flow state that shares many features of the rotor vortex ring state.

1 Introduction

The vortex ring state (VRS) of a rotor wake is a dangerous operating condition that generally occurs under certain conditions of powered descent, and requires special operating procedures for the helicopter pilot to avoid and fly out of. It is also a fascinating fluid dynamic phenomenon, and this paper concentrates on this aspect of the VRS. In the vortex ring state, the helical vortex wake that is normally trailed below a rotor collapses into a highly unsteady, toroidal vortex system, which remains in the vicinity of the rotor disc and has a diameter at least as large as the rotor itself. This results in large thrust oscillations and so-called power settling, where application of more power fails to generate additional lift. Knowledge of the phenomenon is almost as old as the helicopter itself, and the remarkable demonstration of smoke flow past a model helicopter by [4] is a notable, early contribution to the field. Further early experimentation concentrated upon the practical rotor performance aspect of the VRS, for example [12]. VRS received relatively little attention until more recently, and renewed interest in the problem triggered various experimental studies, for example [2] and [6], that revealed flow patterns below and around the rotor and the accumulation of trailed vortices around the edges of the disc. The unsteadiness of the flow field is a key feature of the VRS, and [10] were able to correlate the thrust oscillations with the flow patterns in VRS. More recent work by [8] was able to correlate the thrust oscillations with the phasing of the wake vorticity dynamics. This work concentrated on non-axial descent where the greatest thrust oscillations were observed, and used Particle Image Velocimetry (PIV) to help observe the vortex filaments and their fate during the VRS thrust oscillation. While the vorticity over the leading edge area of the disc formed a tight bundle that contracted and enlarged during the thrust cycle, with lower thrust levels correlating with the break up of the bundle, the vorticity around the trailing edge revealed a continuous formation and breakdown of a large vortex structure. High thrust was associated with vortices trailing below the disc, while decreasing and low thrust occurred as vorticity accumulated around the trailing edge itself, a condition similar to that seen in axial descent in the VRS. Interaction of individual filaments was of interest, with incidences of pairing and leapfrogging of vortices observed. Computational modelling has been challenging owing to the need to preserve vortices for long non-dimensional times, and free wake methods and computational fluid dynamics techniques have been set up that have shed light on the phenomenon ([3], [1]). [7] and [3] in particular were able to suggest that a non-linear coupling between the rotor loading and flow perturbations drove a global destabilisation of the rotor wake leading to the flow topology observed in the VRS. The dynamics and stability characteristics of helical vortices have been investigated for many years, [11], and the observations of VRS would tend to suggest that the stability of the helical vortex filaments in the rotor wake play a critical role. On the other hand actuator disc theory has been a useful tool for the treatment of the phenomenon, for example [9], where a failure of the streamtube model is associated with the onset of the VRS.

It is intriguing that actuator disc theory, a low-order momentum theory model, can be so useful in the description of the VRS, and this leads one to question the role of the trailing vortex system. With the VRS considered as a problem for rotorcraft, any computational or experimental study has necessarily required the use of a rotor system, either simulated or physical. In actuator disc theory there is a pressure jump across a notional discontinuity that represents the rotor disc, and a streamtube contains the disc and the fluid mass that passes across it. The cause of the actuator disc pressure jump is non-specific, but it is analogous to what happens with real rotor blades, where the pressure on the lower surface of a blade is greater than the upper surface. The edge of the streamtube in actuator disc theory is a discontinuous vortex sheet, but it contains no discrete vortex filaments, and the actuator disc model is an extreme simplification of the actual flow, in which the rotor blades trail a vortex sheet that rapidly rolls up to

form root and tip trailing vortex filaments. Given the simplicity of actuator disc theory, it is interesting to consider the role of the trailing vortex filaments and the presence of the rotor blades (or equivalent vorticity sources) in the flow, and to establish their importance in the occurrence of the VRS. This paper aims to shed some light on this by considering an experimental investigation of a jet system that produces a mean flow similar to the mean flow in a rotor wake, but has no rotor blades and hence no distinct trailing vortex filaments. The jet injects momentum into the flow, but is allowed to induce flow in a similar manner to a rotor. The experimental system is described, and results of the onset of a VRS-like flow field are presented and compared with results from experiments conducted with traditional rotor systems.

2 Experimental method

The experiments comprised tests on a jet system that provides a mean flow analogous to that for a rotor wake, and on rotor flows. PIV was used as the main experimental method. The various systems are described in this section.

2.1 Open core, annular jet system as an analogue to a rotor flow

An experimental analogue of the rotor wake mean velocity profile was generated using a specially designed, open core, annular jet system shown in figures 1 and 2. The design is based on a so-called air amplifier used for industrial applications. It consists of a plenum chamber in the form of a hollow toroid with an aerofoil-like cross section. An annular slot runs around the radially inward facing surface of the toroid, allowing air pumped into the plenum chamber to flow out of the gap to form a jet. The annular slot therefore generates an annular jet with the radially outward portion bounded by the inward surface of the toroid, while the inward side of the jet forms a free shear layer. The jet follows the inward facing toroid surface by Coandă effect, but the free shear layer of the jet entrains air. This aspect of the jet behaviour induces air flow u_i through the hole of the toroidal ring. The term 'annular jet' in the literature appears to refer to the jet flow through an annular orifice formed by a circular, solid plug fitted concentrically inside a circular jet orifice. This is quite different from the jet flow described in this paper, the major difference being the open boundary in the middle of the toroid that air is free to move across, so for the purposes of this paper the jet system is described as an open core, annular jet. Referring to figure 2 the ring diameter D at the toroid trailing edge was chosen to be $D = 0.15$m (radius $R = 75$mm) on the basis of previous VRS experiments conducted in the same wind tunnel ([5]). The chord length of the toroid was 70mm, the thickness of the aerofoil cross-section was 20%, and the depth of the gap forming the jet orifice was 2mm. Air was pumped into the toroid plenum chamber through a pipe that acted as the support in the wind tunnel. A Kiel probe was placed in the pipe to allow the mass flow rate into the plenum chamber to be monitored. The jet exit velocity at the gap was estimated using a small Pitot probe, and at the experimental settings used it was 25ms^{-1}, giving a Reynolds number based on gap width of 3,300. Flow visualisation indicates turbulent flow just after the gap and PIV at the exit plane shows highly unsteady flow in the jet shear layer.

A sketch of the mean flow across the trailing edge plane of the ring is indicated on figure 2, and it shows the expected jet velocity profile due to the jet orifice, but with the inner core flow induced by the jet entrainment. This jet system develops downstream; the turbulent shear layers diffuse outward into the undisturbed outer flow, and inwards towards the axis of the toroid. The effect is to produce a jet flow with mean flow characteristics similar in topology to the *mean* flow below a rotor, but this has been achieved by direct mass and momentum injection into the flow rather than by lift induced flow through a rotor disc. There is no helical vortex wake, so the stability characteristics of the flow are not dependent upon the dynamics of such a system. Results showing the velocity profile will be presented in a later section.

2.2 Wind tunnel tests of simulated VRS

VRS can be simulated in a wind tunnel by using a rotor system thrusting against the wind tunnel flow, with the wind tunnel speed U_∞ acting as the simulated descent rate V_d. Wind tunnel experiments were performed in the University of Glasgow low-speed, closed return wind tunnel with a 1.05m $\times$ 0.85m working section and turbulence level of some 0.3%. The rotor system used for the wind tunnel simulation of VRS was based on the thrusting propeller model described by [5]. A three-bladed, twisted rotor of radius R=75mm was placed in the wind tunnel, with rotor axis parallel to the flow direction. The rotor was powered by a D.C. electric motor, mounted at the end of a long, slender shaft, and fastened to a faired support affixed to the wind tunnel floor. The rotor was operated at a rotational speed of 120 Hz for all cases, equivalent to a blade tip speed of $V_{tip} = 56.5$ms^{-1}, giving a representative chord Reynolds number 46,000 based on tip velocity and geometric mean chord.

Prior to wind tunnel testing and in order to normalise the respective simulated descent rates of the rotor and open core, annular jet, the induced velocity generated by each was calculated, allowing for the results to be presented in a consistent manner. Static rotor thrust T was measured using a load cell, the result of which gives a thrust coefficient $C_T = \frac{T}{\rho A V_{tip}^2} = 0.014$, where ρ and A are the ambient air density and rotor disc area respectively, and from which the hover induced velocity at the rotor disk was determined as $V_h = V_{tip}\sqrt{C_T/2} = 4.7$ms^{-1}, and this was used as the scaling velocity for the rotor experiments in the wind tunnel. An equivalent hover induced velocity for the open core, annular jet was determined by integrating the momentum and mass flux across the trailing edge plane of the jet, and the equivalent uniform induced velocity V_i across the trailing edge plane then provided the same momentum for the same mass flow rate giving $V_i = 1.8$ms^{-1}. This was used as the scaling velocity for the open core, annular jet experiments.

2.3 Flow field measurement of the wind tunnel experiments

The main experimental method used was two-component PIV, which is able to capture the spatial features of the flow, but limited flow visualisation experiments were performed using

a smoke wand, high speed camera and a stroboscope. The PIV system employed in this investigation used a Spectra Physics Lab-130-10 Nd:YAG laser for illumination and a Redlake Megaplus ES4.0 digital video camera of 2048 × 2048 pixel resolution fitted with a 100 mm focal length lens. The camera was trained on an 18cm × 18cm wide field of view at various locations in the symmetry plane of the flow. The light sheet was produced using beam shaping optics, mirrors and a cylindrical lens and delivered into the working section of the wind tunnel from above. Seeding for the PIV system was produced by a smoke generator, which used an electrical heater to heat commercial smoke oil to produce a fine mist that was pumped in to the wind tunnel using carbon dioxide. The nominal seeding particle diameter was less than 1μm. The PIV analysis methodology was based on cross-correlation and employed a window shifting feature for outlier vector detection and resolution. Window over-lapping, window reduction and window shifting were used to achieve high resolution and mitigate against digital correlation peak locking. 144 individual samples per case were recorded; while the wind tunnel PIV was not time resolved, this many samples permits a meaningful calculation of mean flow, and the unsteady flow characteristics can be investigated by computation of the root-mean-square of the velocity and by correlation analysis of individual results.

The velocity profile of the annular jet system outside the wind tunnel was also investigated with a Dantec 2D FiberFlow two-component Laser Doppler Anemometry (LDA) system. Measurements were taken along radial lines in the symmetry plane at various distances away from the jet exit plane, from as close as 4mm to one radius away, and the radial step distance was $\Delta r = 2$mm. The LDA probe was mounted on a 3-axis traverse system so that the velocity components measured by the LDA system were the axial and the radial velocity components. Two 1W diode pumped solid-state lasers were used with wavelengths respectively of 514.5 nm (green) and 488 nm (blue). The probe diameter was 112 mm and fitted with a 1.5 ratio beam expander, giving a focal length of 1200 mm and a beam diameter of 4.1 mm and measurement volume ellipsoid dimensions of $2.62 \times 0.12 \times 0.12\text{mm}^3$. Beam splitting and 40 MHz frequency shifting by a Bragg cell were provided by the system, and the signal from the light-scattering particles was collected and processed by a commercial burst spectrum analyser (BSA F60 Flow Processor) and Dantec BSA Flow software v5.02 which provided measurement and traverse system control also. Seeding was generated by a PS27 smoke machine with particle diameter of 0.2-0.3 micron. For every measurement position, 10000 valid samples were taken, ensuring a 95% confidence limit of the mean value and under 0.01ms^{-1} for most of the cases with a maximum of 0.04ms^{-1} around the jet peaks.

2.4 Water tank measurements of VRS

Data are available from the experiment described by [8], which used a $D = 0.254$m diameter, three-blade rotor towed through water along the length of a 67 m long × 2.4 m wide × 1.65m deep towing tank at the University of California, Berkeley. The rotor was designed to perform well at the low chord Reynolds number, and had 5^o linear twist, constant chord $c = 1.9$cm, and used interpolated blade sections from ARA-D-10 at the tip to modified ARA-D-13 at the root. The notional chord Reynolds number was 60,000. Phased (strobed), two-component PIV using a 1 Mpixel digital video camera and pulsed Nd:YAG laser and thrust measurement were used to correlate flow state with thrust oscillations. PIV analysis was performed by cross-correlation with a Lagrangian parcel tracking algorithm that allowed for window deformation in areas of high shear. Experiments were performed with the rotor descending over a range of descent angles and speeds, with descent angle $\alpha = 90^o$ corresponding to axial descent. For a rotational speed of 4rev/s the hover thrust coefficient was $C_T = 0.01$, giving a hover induced velocity of $V_h = 0.226\text{ms}^{-1}$.

3 Results

PIV results for all cases are presented with the light sheet in the geometrical symmetry plane of the flow. The field of view was positioned at various locations in the flow field depending on the area of interest. Length scales are referenced to the rotor radius or toroid exit radius R, and velocity scales are referenced to the rotor hover induced velocity V_h or the annular jet equivalent induced velocity V_i. The coordinate system for the PIV results presentation is shown in figure 3; r is the rotor or toroid radial ordinate, y the vertical position along the rotor or toroid axis (negative y is below the rotor disc or toroid exit plane). A typical field of view is shown, and this is coincident with the (r, y) plane. Accuracy of the PIV depends on a range of factors and what is required from the experiment. The intention in these experiments is to visualise and quantify the gross flow features. Spatial velocity gradients in these flows are intense, so absolute accuracy of the PIV is compromised when the field of view is as large as in these experiments. For the wind tunnel measurements the PIV resolution was better than $0.039R \times 0.039R$, while for the water tank experiments the resolution was $0.02R \times 0.02R$, and in both cases this is enough to resolve the presence of vortices trailed from blade tips or the presence of the jet at the toroid exit plane. The water tank data are inherently more accurate in spite of the lower relative camera resolution, simply because much larger tracer particles may be used in water compared to air. Spatial calibration errors for both experiments are negligible. Velocity accuracy is estimated to be better than 2%, but while there is inevitable data loss in regions of high shear where the large field of view reduces resolution, there is sufficient resolution to identify the presence and sense of features as small as trailing vortices. For the wind tunnel PIV vorticity was determined using the least squares algorithm best suited to PIV data, while vorticity for the towing tank PIV was obtained by a spectral method.

Description of the rotor wake VRS flow field will be presented followed by the behaviour of the open core, annular jet in simulated descent. PIV results are presented as mean flow with some unsteady flow statistics shown as root-mean-square velocity where appropriate. Instantaneous PIV results are only shown to illustrate specific points.

3.1 Wind tunnel tests of the rotor wake in VRS

The results shown in this section broadly show the flow following the trend described by [5]. Figure 4 shows the rotor flow mean velocity field below the rotor in hover and at increasing descent rate into deep VRS at $\frac{V_d}{V_h} = 1.63$. An approximately 1-diameter square region shows the flow from close to the rotor axis to beyond the edge of the disc and from just above the disc to well below it. Mean velocity fields are shown, and although the flow is highly unsteady the results presentation serves to illustrate the change in gross flow topology. Mean flow particle pathline plots are presented in figure 5 to aid interpretation of the velocity field figures. The hover flow field in frame (a) of each figure shows the basic tubular flow field topology for hover (note that the trailing vortices are not evident as the averaging process has smeared them out). No outboard pathlines are shown as the velocity there is so low. As descent rate increases, frame (b), changes to the flow inboard of the tip of the disc are subtle, but further outboard the opposing descent rate velocity is evident by the up-flow in the $\frac{r}{R} = 2$ region. Frame (c) at $\frac{V_d}{V_h} = 1.15$ shows up-flow on the right of the field of view, down-flow below the rotor, but a mean flow recirculation centred around $\frac{(r,y)}{R} = (1.5, -1)$. The next frame (d) is more dramatic; at $\frac{V_d}{V_h} = 1.35$ the recirculation region is almost level with the plane of the disc, the flow below the rotor turns outboard, and there is a mean flow pathline saddle point at $\frac{y}{R} = -1.7$ (not shown) where the mean flow velocity magnitude is very low. Following a further increase in the descent rate the saddle point moves towards the disc and the mean flow recirculation zone moves further up, and at sufficiently high descent rate, such as frame (e) at $\frac{V_d}{V_h} = 1.68$, upflow penetrates right up to the disc and the mean flow recirculation zone forms above the plane of the disc.

3.2 Wind tunnel tests of the open core, annular jet in VRS

Figures 6 and 7 present mean flow velocity and pathlines for the open core, annular jet in a similar manner to the the results for the rotor in figures 4 and 5. Descent rates were selected to show similar trends for each flow. The hover case for the jet, frame (a) in each figure, shows that the annular jet mean flow has the same tubular topology as the rotor mean flow, and the only remarkable difference is that the pathlines diverge outboard in the annular jet case, and this is due to the entrainment by the turbulent jet. The major structural difference is the mean flow vorticity, where the core flow of the annular jet is irrotational, whereas for the rotor substantial vorticity is trailed at the blade root area (vorticity will be discussed further in a later section). Frames (b) to (e), showing increasing descent rate, show similar changes to the flow field as for the rotor, but upward flow penetrates right up to the exit plane quite readily. For example compare figure 7 frame (d) with figure 5 frame (d) where the mean recirculation zone is at almost at the same height but the rotor shows no upflow. Frame (c) for the annular jet suggests that the mean recirculation flow first forms far outboard also.

3.3 VRS tests in the towing tank

Representative results from the towing tank tests are shown in figure 8. Frame (a) for hover shows a very similar mean flow pathline plot compared with the wind tunnel rotor test case. Pathline curvature around $r = 0$ is due to the relatively large diameter shaft supporting the rotor. Frame (b) shows the rotor in VRS at a lower, but comparable, non–dimensional descent rate than for the wind tunnel tests, and it is seen that the mean flow topologies are similar.

4 Discussion

The results presentation has concentrated upon the flow below and on one side the rotor. [5] described how the flow in this region correlated with flow topology changes elsewhere, and the formation of the mean flow recirculation can be observed in this field of view anyway. The changes to the mean flow pathlines as descent rate increases for the three experiments show broad similarities; the tubular downflow widens, an outboard recirculation region becomes evident that moves upward with increasing descent rate, and upward flow penetrates up to the rotor disc or jet exit plane. The annular jet flow appears to develop the upward flow more readily, when the recirculation zone is less compact. Elements of this discussion will concentrate upon the similarities and differences between the rotor and annular jet flows.

4.1 Details of the open core, annular jet

It is helpful to examine the open core, annular jet flow in more detail. The mean flow velocity vector and pathline diagrams help to reveal flow topology, but they hide fine features. Given the context of this paper, it is instructive to look at how the annular jet flow compares to the rotor flows. Figure 9 shows the non-dimensional axial flow v-component plotted against radial distance for (a) the LDA survey at various axial distances y and (b) for the rotor flows and annular jet PIV at $y/R = -1$ below the rotor. The LDA survey shows the evolution of the jet with distance from the exit plane, and the peak velocity falls and jet width increases as expected. Frame (b) showing PIV data indicates that the two rotor experiments have similar velocity profiles to each other, with the minimum velocity location substantially inboard of $r/R = 1$. The annular jet shows a quite different looking profile, with minimum velocity occurring at around $r/R = 1$, and further inboard the velocity magnitude falls rapidly to a constant value for $r/R < 0.5$. Note that the two rotor flows do not show this inboard uniform velocity region. The rotor and annular jet flows are notionally axisymmetric, so the plots can be rotated around r/R =0, and it is then clear that the rotor flow differs from the annular jet in that there is continuous shear for r/R <1 in the flow below the rotor, while for the annular jet the shear is confined to the extent of the jet only and the induced flow in the core is at uniform velocity albeit reducing in magnitude with greater distance below the exit plane. Both rotor and annular jet flows, however, are topologically similar in that there is a maximum velocity around r =0, decreasing to a minimum as r increases and then increasing further outboard to zero.

The rotor flows produce their highest magnitude v-component inboard of r/R =1 because the downward convecting trailing vortices produce a higher downward velocity on the inboard side of the vortices, and this effect is enhanced by the vortex system trailed from the blade root area generating a higher velocity to the outboard side of the vortices. The annular jet flow, on the other hand, produces the downflow from the initial momentum of the jet and its subsequent diffusion and entrainment. Vorticity for the annular jet and a comparison with the rotor flows is shown in figure 10. The vorticity for the annular jet shows the presence of the jet shear layer, and adjacent regions of negative and positive vorticity are simply the result of the shape of the jet velocity profile. Outside the jet the flow is irrotational, and the core flow is irrotational. Frame (b) of the figure compares the mean flow vorticity along the line $y/R = -1$, and the averaging process filters out the individual trailed vortex contributions for the rotors. Peak positive and negative vorticity for the annular jet is farther outboard than for the rotors, but the rotor flows have no region of irrotational flow inboard of r/R =1, and this is the only significant difference in the flow fields in terms of mean flow vorticity. Both the rotor and annular jet flows are unsteady, and this unsteadiness is usefully described by the root-mean-square (RMS) velocity. The sample size of 144 velocity maps per test case. A comparison of the rotor and annular jet flows showing the RMS velocity as a function of radial distance at y/R =-1 is given in figure 11. Both rotor flows have similar distributions, with the outboard peak around r/R =0.75 due to the passage of the tip vortices, and the high RMS value inboard due to the passage of the root vortex system. The annular jet RMS velocity is quite different, with a broad peak in the jet and very low values in the core and external flows.

From the above it can be seen that there are broad similarities in the mean flow topologies of the rotor and annular jet flows. Both show the maximum velocity magnitude lying below the outer portion of the disc/ exit plane, and regions of strong, oppositely signed vorticity lie next to one another.

4.2 Evolution of Vortex Ring State for the open core, annular jet

[5] showed how the rotor wake flow evolved from the hover case into deep VRS as the descent rate increased. The flow was observed to be highly unsteady everywhere, but at intermediate descent rate their analysis established that the unsteadiness was fundamentally one of the flow switching from a topology similar to hover, to one similar to deep VRS, and back again, with a greater likelihood of the flow being in a deep VRS state at the higher descent rate. They used a correlation analysis of their PIV data, and it is worth repeating this for the current, open core, annular jet flow. The flow topology in hover is straightforward, and the mean flow hover case shown in frame (a) of figures 6 and 7 provides the correlation template for hover. There are two distinctive features in the VRS flow field, upflow penetrating right up to the exit plane of the annular jet, and the mean flow recirculation outboard, and the mean flow VRS case at descent rate $\frac{V_d}{V_i} = 1.1$ shown in frame (d) of figures 6 and 7 provides a suitable VRS correlation template. Velocity data from individual PIV snapshots at an intermediate descent rate can be cross-correlated with the PIV mean velocity templates for hover and VRS. Normalised correlation coefficients of individual PIV snapshots with the templates are shown in figure 12. The data are sorted according to the difference between the two correlation coefficients, and it can be seen from the extreme ends of the plot that cases that correlate well with one mean flow correlate very poorly with the other mean flow. In the middle of the distribution the correlation with either template is moderate. Representative individual PIV snapshots from each of the extreme ends of the correlation plot showing velocity and instantaneous streamlines are shown in figure 13, and comparison with the annular jet mean flow hover and deep VRS velocity fields and mean flow pathlines shown in figures 6 and 7 frames (a) and (d) reveals the usefulness of this analysis. Note that *none* of the individual PIV snapshots at the highest descent rate of $\frac{V_d}{V_i} = 1.5$ show any positive correlation with the hover template. An interesting case to consider is when an individual PIV snapshot correlates equally well with both hover and VRS, and such a case is shown in figure 14 with correlation coefficient value of 0.55 for both hover and VRS. It has features of both hover and VRS, *viz* outboard down flow and inboard up-flow respectively. Note the clockwise rotating feature centred around $\frac{(r,y)}{R} = (0.6, -0.4)$; this is a typical transient concentration of negative vorticity, and flow visualisation shows this feature forming and being ejected downwards. The correlation analysis raises the question of the periodicity of the flow. Flow visualisation shows that the annular jet flow is highly three-dimensional and lacks a distinct periodicity, although the phenomena evolve slowly, equivalent to less than one cycle per second or a non-dimensional frequency of 0.08 based on velocity V_i and exit diameter D. Note that [10] reported a relative lack of periodicity in axial descent for the towing tank rotor flow VRS tests described in this paper.

5 Conclusions

The fluid dynamics of the vortex ring state have been investigated through a series of experiments on rotors and an open core, annular jet flow. Results of wind tunnel and water tank tests on rotors have been compared with the jet flow. The topological details of the mean flows in hover are similar, and in simulated descent the open core, annular jet flow evolves into a vortex ring state that exhibits the key features of the rotor wake vortex ring state.

Copyright statement

References

[1] M.J. Bhagwat and J.G. Leishman. On the aerodynamic stability of helicopter rotor wakes. *56th AHS' Annual Forum, Virginia Beach, VA, USA, 2nd-4th May*, 2000.

[2] P. Brinson and T. Ellenrieder. Experimental investigation of the vortex ring condition. *24th European Rotorcraft Forum, Marseille, France, paper TE13*, 1998.

[3] R.E. Brown, A.J. Line, and G.A. Ahlin. Fuselage and tail-rotor interference effects on helicopter wake development in descending flight. *60th Annual Forum of the American Helicopter Society, Baltimore, MD, USA, 7th-10th June*, 2004.

[4] J.M. Drees and W.P. Hendal. Airflow patterns in the neighbourhood of helicopter rotors. *Journal of Aircraft Engineering*, 23(266):107–111, 1951.

[5] R.B. Green, E.A. Gillies, and R.E. Brown. The flow field around a rotor in axial descent. *Journal of Fluid Mechanics*, 534:237–261, 2005.

[6] J.G. Leishman, M.J. Bhagwat, and S. Ananthan. The vortex ring state as a spatially and temporally developing wake instability. *AHS International Specialists' Meeting on Aerodynamics, Acoustics, Test & Evaluation, San Francisco, CA, USA, 23rd-25th January*, 2002.

[7] S.J. Newman, R.E. Brown, J. Perry, S. Lewis, M. Orchard, and A. Modha. Comparative numerical and experimental investigations of the vortex ring phenomenon in rotorcraft. *Journal of the American Helicopter Society*, 48(1):28–38, 2003.

[8] Ö. Savaş, R.B. Green, and F.X. Caradonna. Coupled thrust and vorticity dynamics during vortex ring state. *Journal of the American Helicopter Society*, 54(2):022001–1 022001–10, 2009.

[9] P.R. Spalart. On the simple actuator disk. *Journal of Fluid Mechanics*, 494:399–405, 2003.

[10] J. Stack, F.X. Caradonna, and Ö. Savaş. Flow visualizations and extended thrust time histories of rotor vortex wakes in descent. *Journal of the American Helicopter Society*, 50(3):279–288, 2005.

[11] S.E. Widnall. The stability of a helical vortex filament. *Journal of Fluid Mechanics*, 54(4):641–663, 1972.

[12] P.F. Yaggy and K.W. Mort. Wind-tunnel tests of two vtol propellers in descent. *NASA TN D-1766*, 1963.

Figures

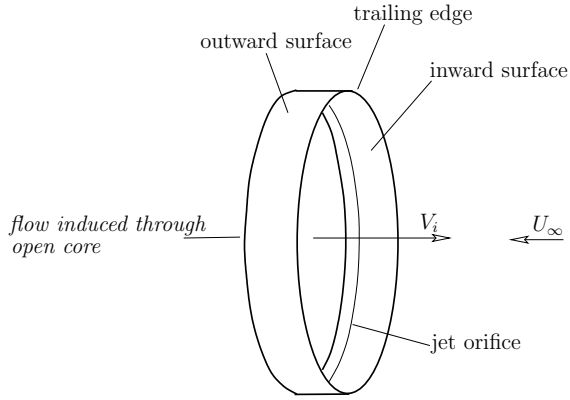

Figure 1: Schematic diagram of open core, annular jet

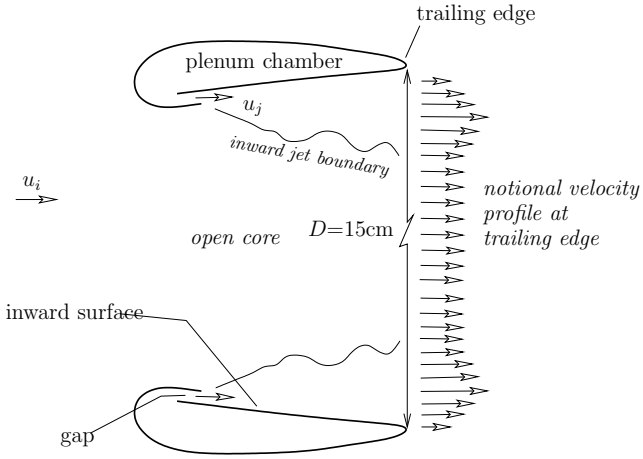

Figure 2: Cross-section through open core, annular jet showing gap on inward side of toroid forming the jet orifice

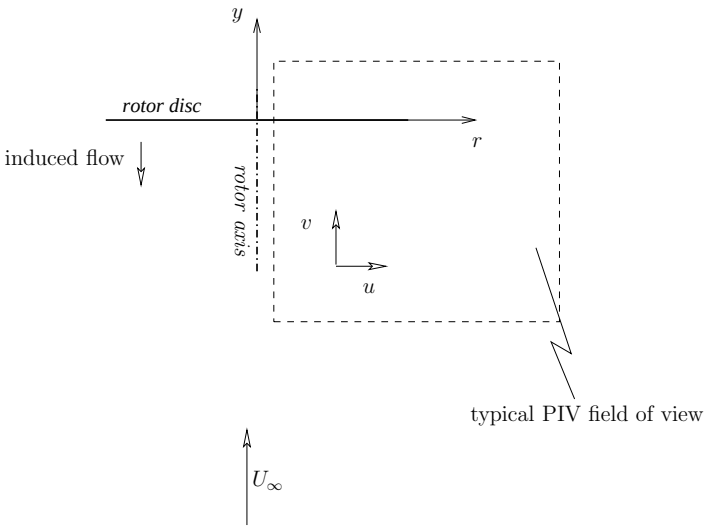

Figure 3: Schematic diagram showing orientation of data for results presentation and the coordinate system used in the paper

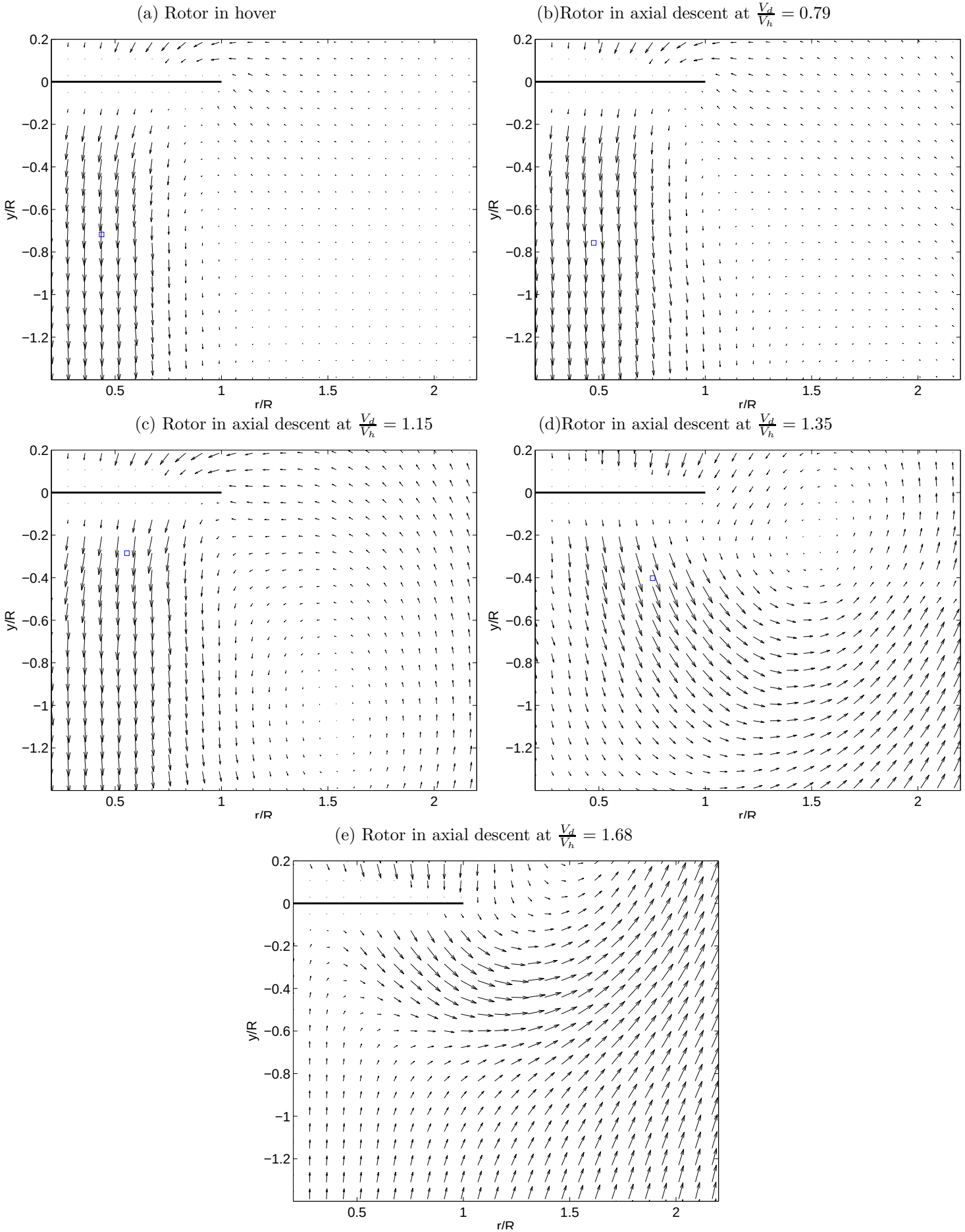

Figure 4: Wind tunnel rotor flow fields (mean velocity) for (a) hover and (b), (c), (d), (e) the rotor in VRS in axial descent at increasing $\frac{V_d}{V_h}$. The origin of the coordinate system is at the centre of the rotor disc, and the thick, black, horizontal line shows the rotor disc.

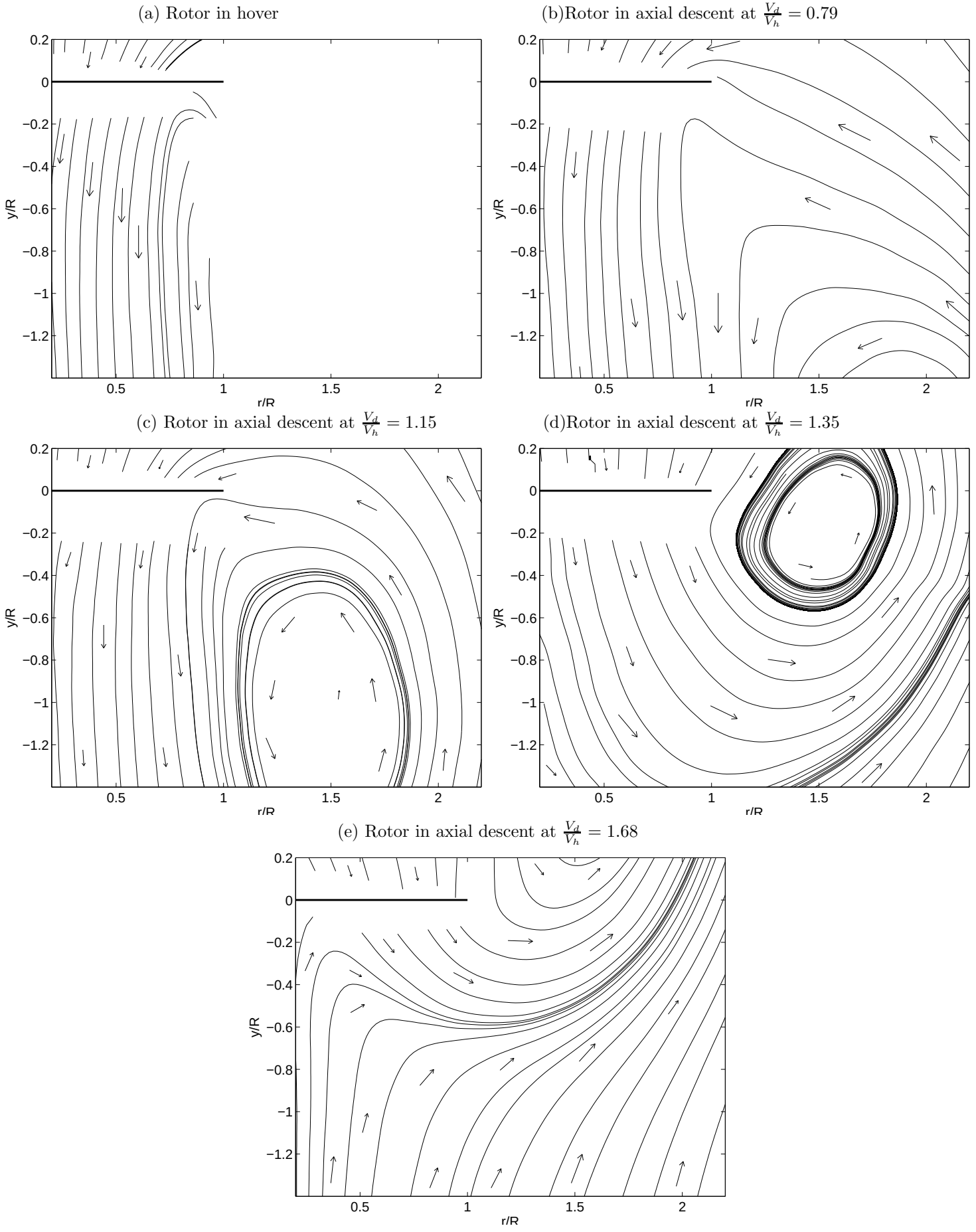

Figure 5: Wind tunnel rotor flow fields (mean flow pathlines) for (a) hover and (b), (c), (d), (e) the rotor in VRS in axial descent at increasing $\frac{V_d}{V_h}$. The origin of the coordinate system is at the centre of the rotor disc, and the thick, black, horizontal line shows the rotor disc in each case. The arrows are drawn on to indicate mean flow direction.

(a) Annular jet in hover

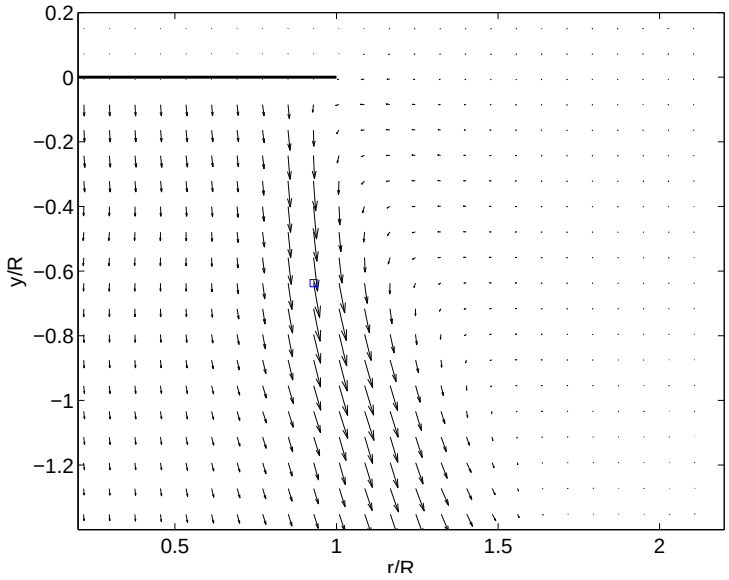

(b)Annular jet in axial descent at $\frac{V_d}{V_i} = 0.5$

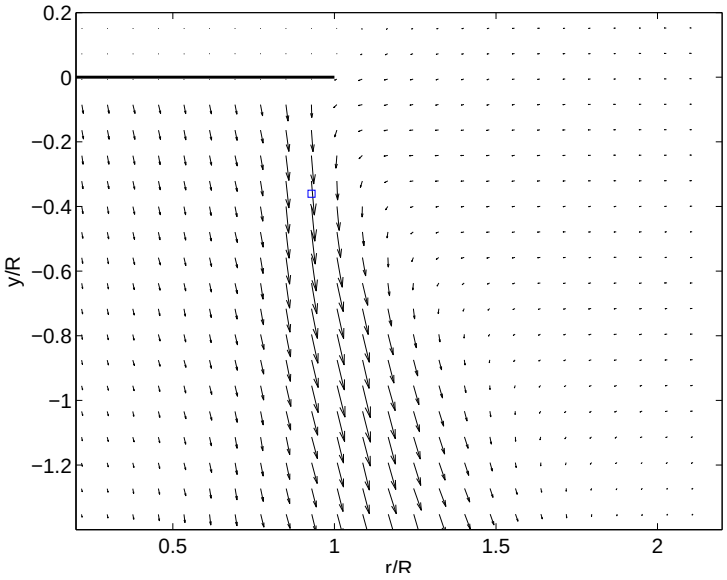

(c) Annular jet in axial descent at $\frac{V_d}{V_i} = 0.73$

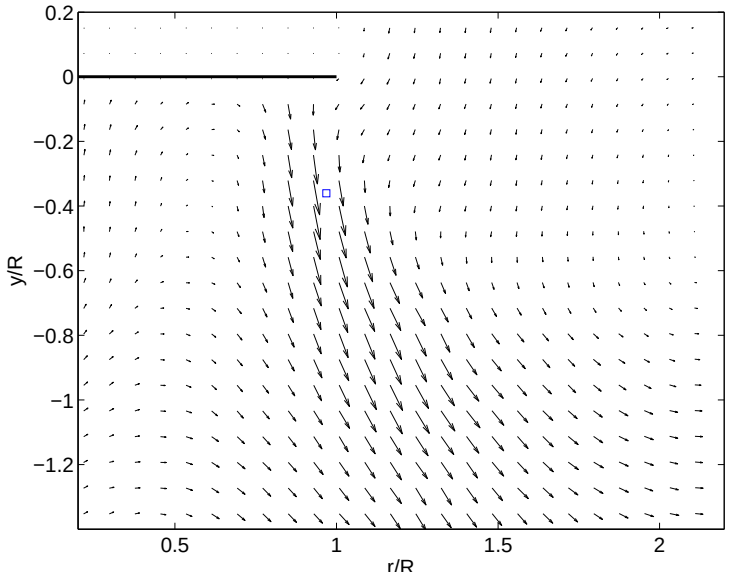

(d)Annular jet in axial descent at $\frac{V_d}{V_i} = 1.11$

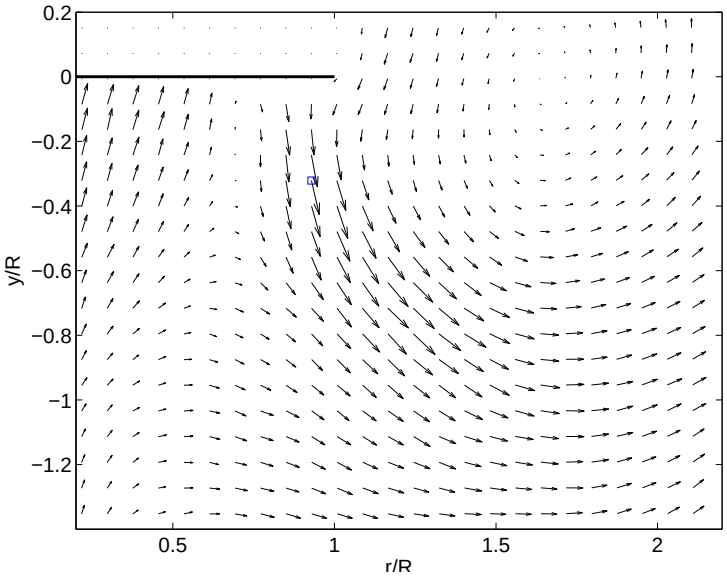

(e) Annular jet in axial descent at $\frac{V_d}{V_i} = 1.5$

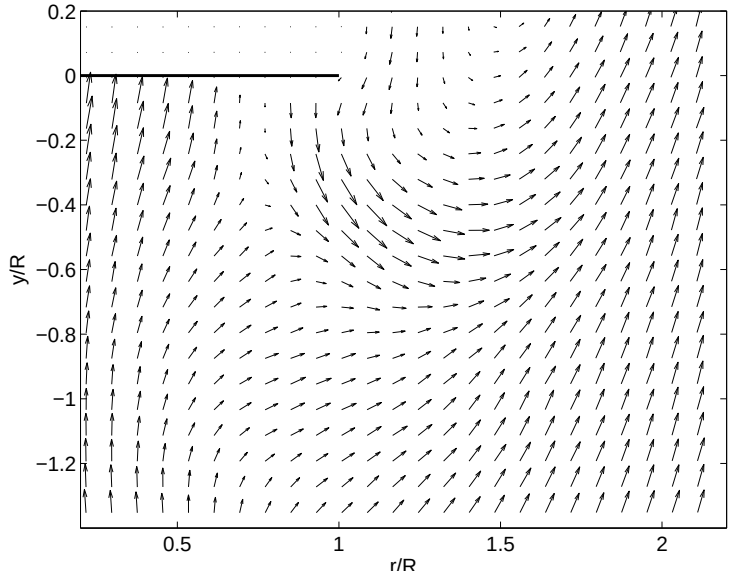

Figure 6: Open core, annular jet flow fields (mean velocity) for (a) hover and (b), (c), (d), (e) the jet in axial descent at increasing $\frac{V_d}{V_h}$. The origin of the coordinate system is at the centre of the exit plane, and the thick, black, horizontal line shows the jet exit plane. The arrows are drawn on to indicate mean flow direction.

(a) Annular jet in hover

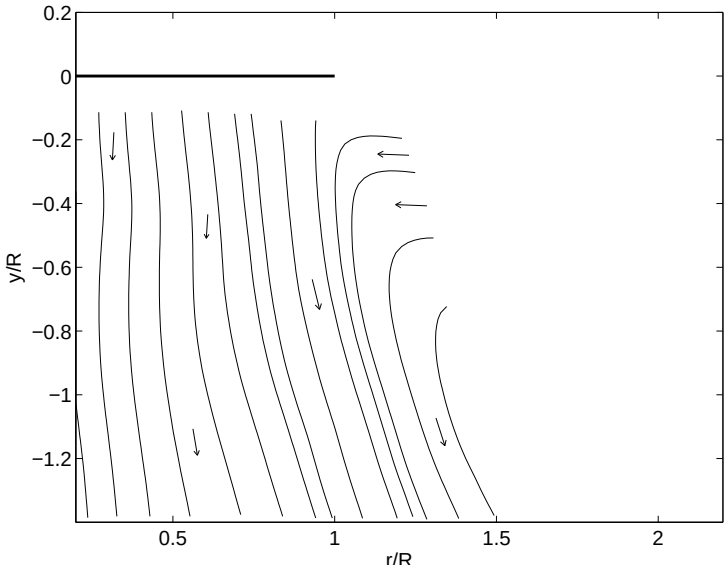

(b)Annular jet in axial descent at $\frac{V_d}{V_i} = 0.5$

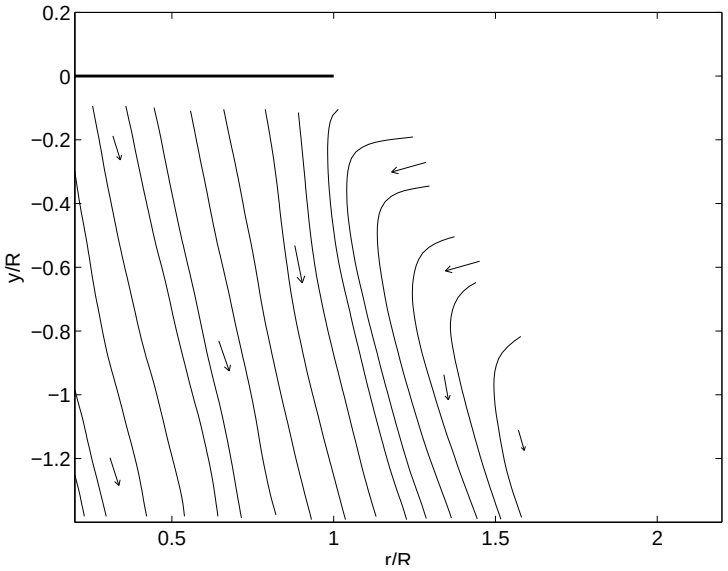

(c) Annular jet in axial descent at $\frac{V_d}{V_i} = 0.73$

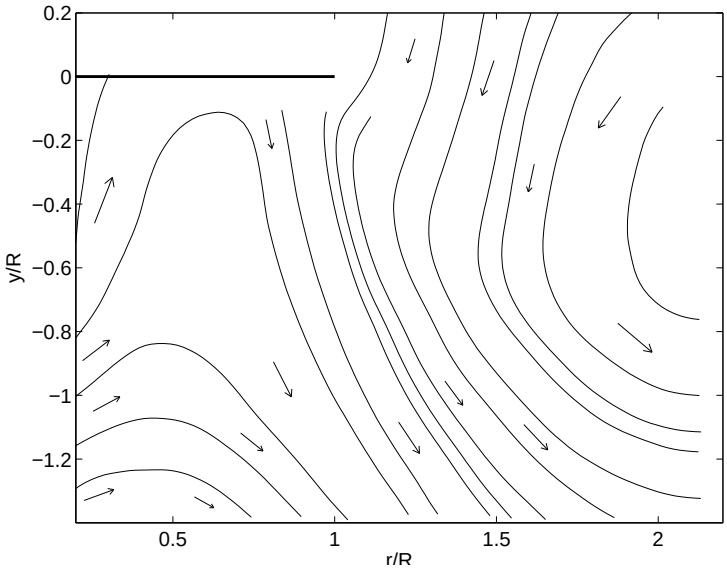

(d)Annular jet in axial descent at $\frac{V_d}{V_i} = 1.11$

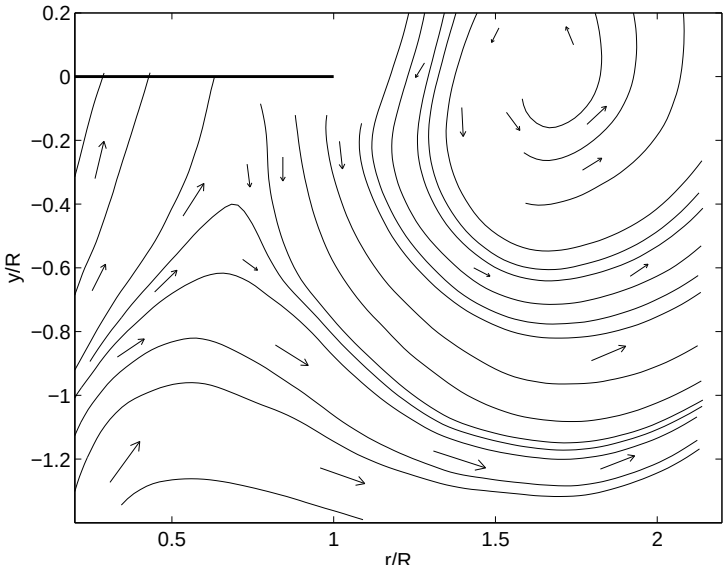

(e) Annular jet in axial descent at $\frac{V_d}{V_i} = 1.5$

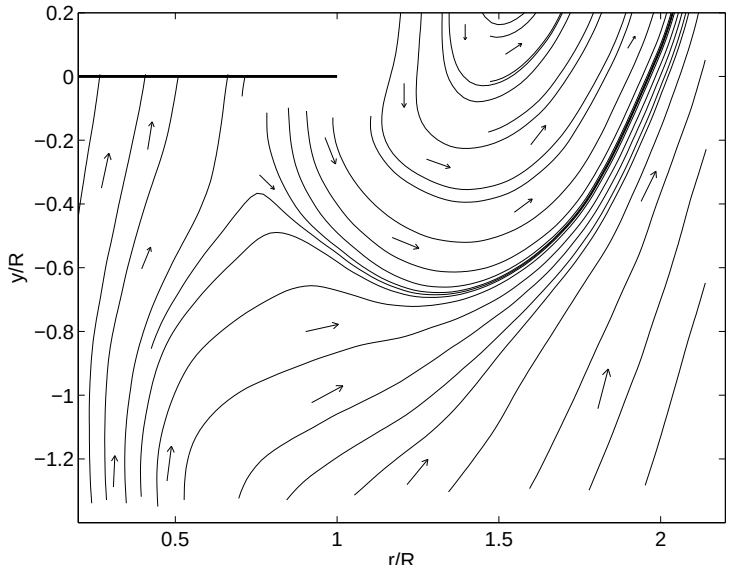

Figure 7: Open core, annular jet flow fields (mean flow pathlines) for (a) hover and (b), (c), (d), (e) the jet in axial descent at increasing $\frac{V_d}{V_h}$. The origin of the coordinate system is at the centre of the exit plane, and the thick, black, horizontal line shows the jet exit plane. The arrows are drawn on to indicate mean flow direction.

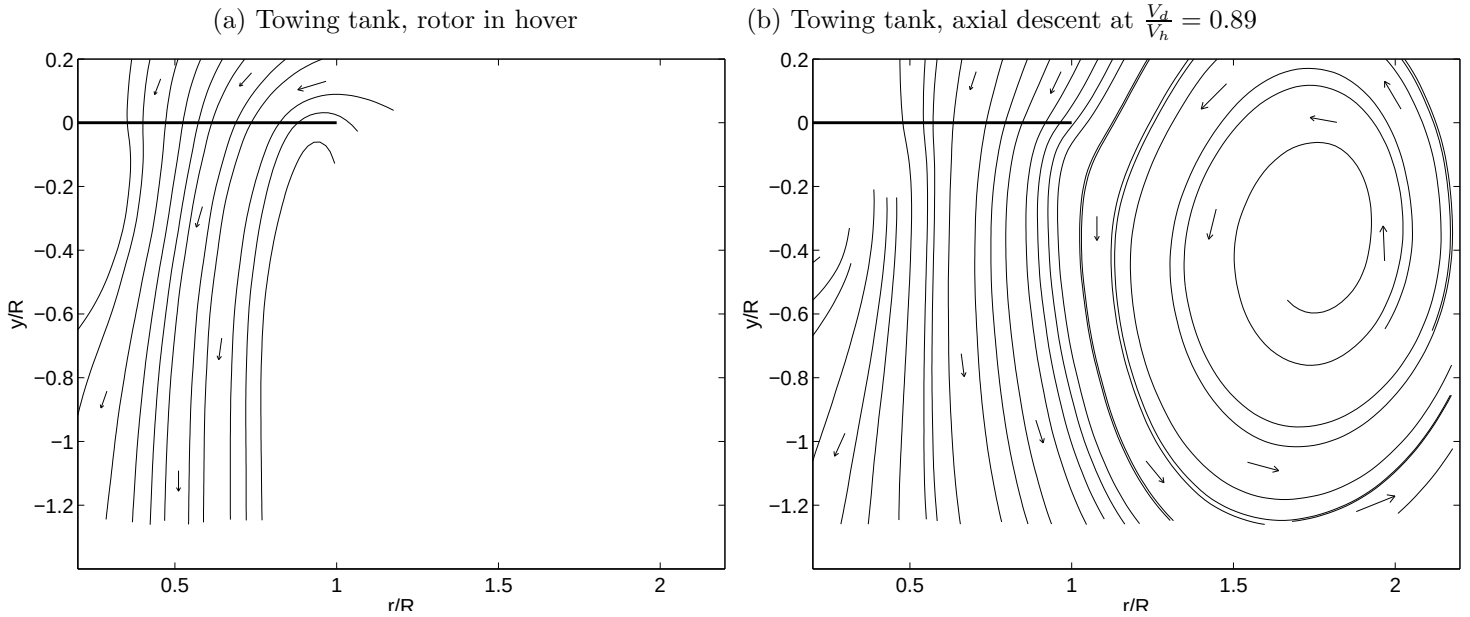

Figure 8: Towing tank rotor flow fields for (a) hover and (b) VRS showing mean flow pathlines. The origin of the coordinate system is at the centre of the rotor, and the thick, black, horizontal line shows the rotor disc.

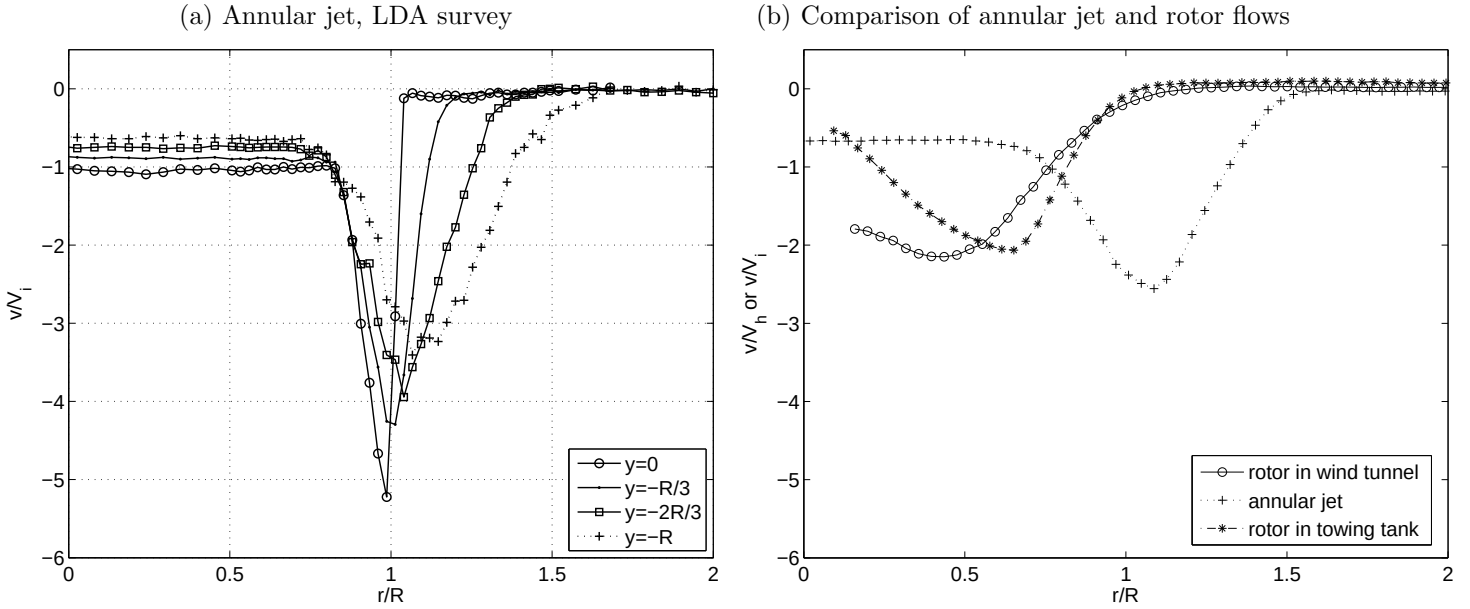

Figure 9: Non-dimensional vertical (axial) component velocity as a function of radial distance for hover. Frame (a) shows LDA data at various positions below the exit plane of the annular jet, and frame (b) shows mean flow PIV data from the annular jet and rotors plotted at $y/R = -1$ below the rotor.

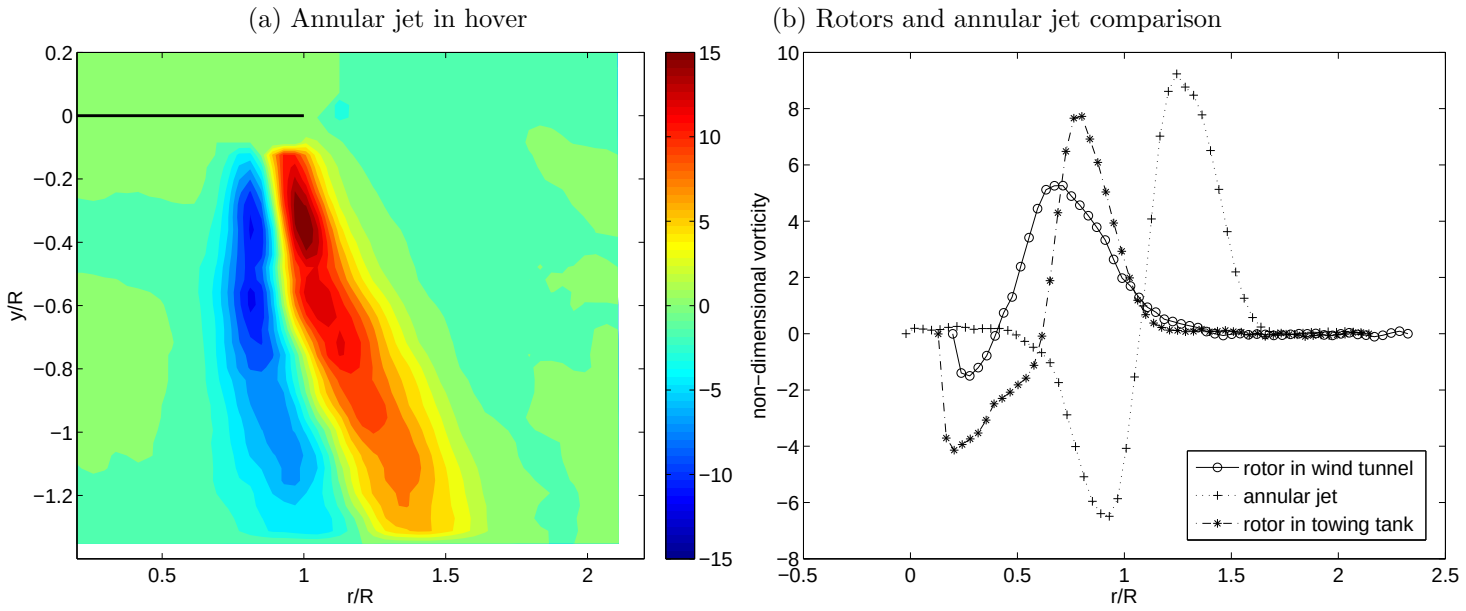

Figure 10: Mean flow field non-dimensional vorticity in hover. Frame (a) shows the annular jet vorticity field, frame (b) shows a comparison of the vorticity along $y/R = -1$. For frame (a) the origin of the coordinate system is at the centre of the exit plane, and the thick, black, horizontal line shows the jet exit plane.

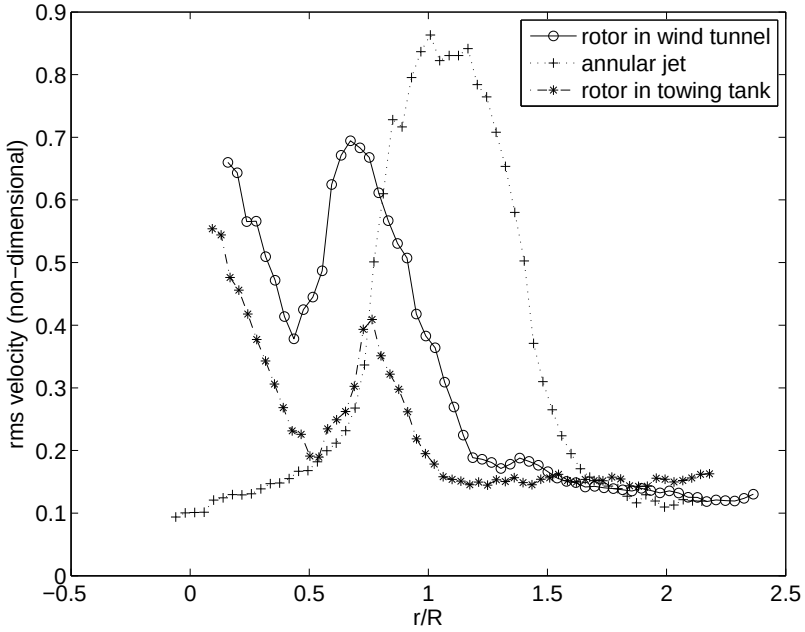

Figure 11: Non-dimensional root mean square velocity as a function of radial distance at $y/R = -1$ below the rotor. Results for the rotor in wind tunnel, annular jet and rotor in towing tank are shown.

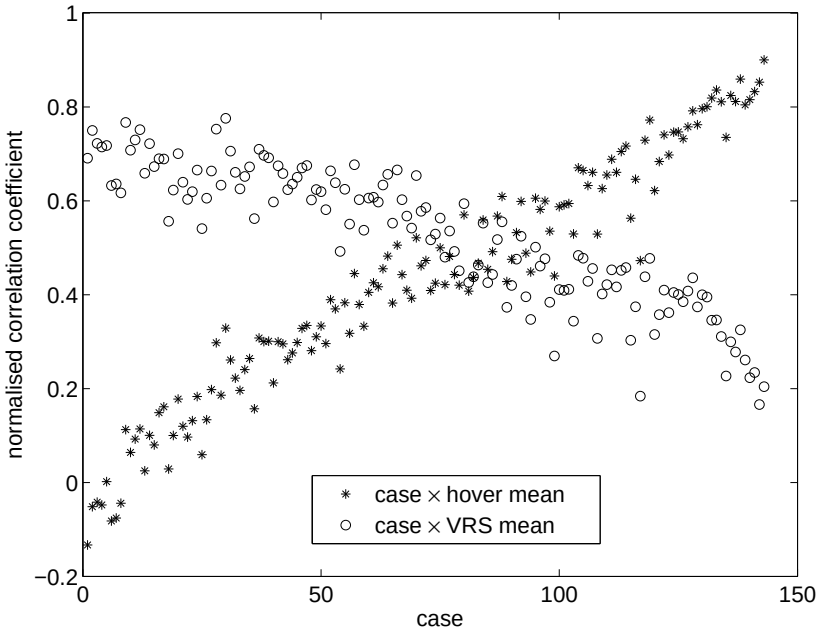

Figure 12: Correlation of annular jet individual PIV snapshots at $\frac{V_d}{V_i} = 0.73$ with mean flow hover and mean flow deep VRS at $\frac{V_d}{V_i} = 1.1$. Normalised correlation coefficients are shown.

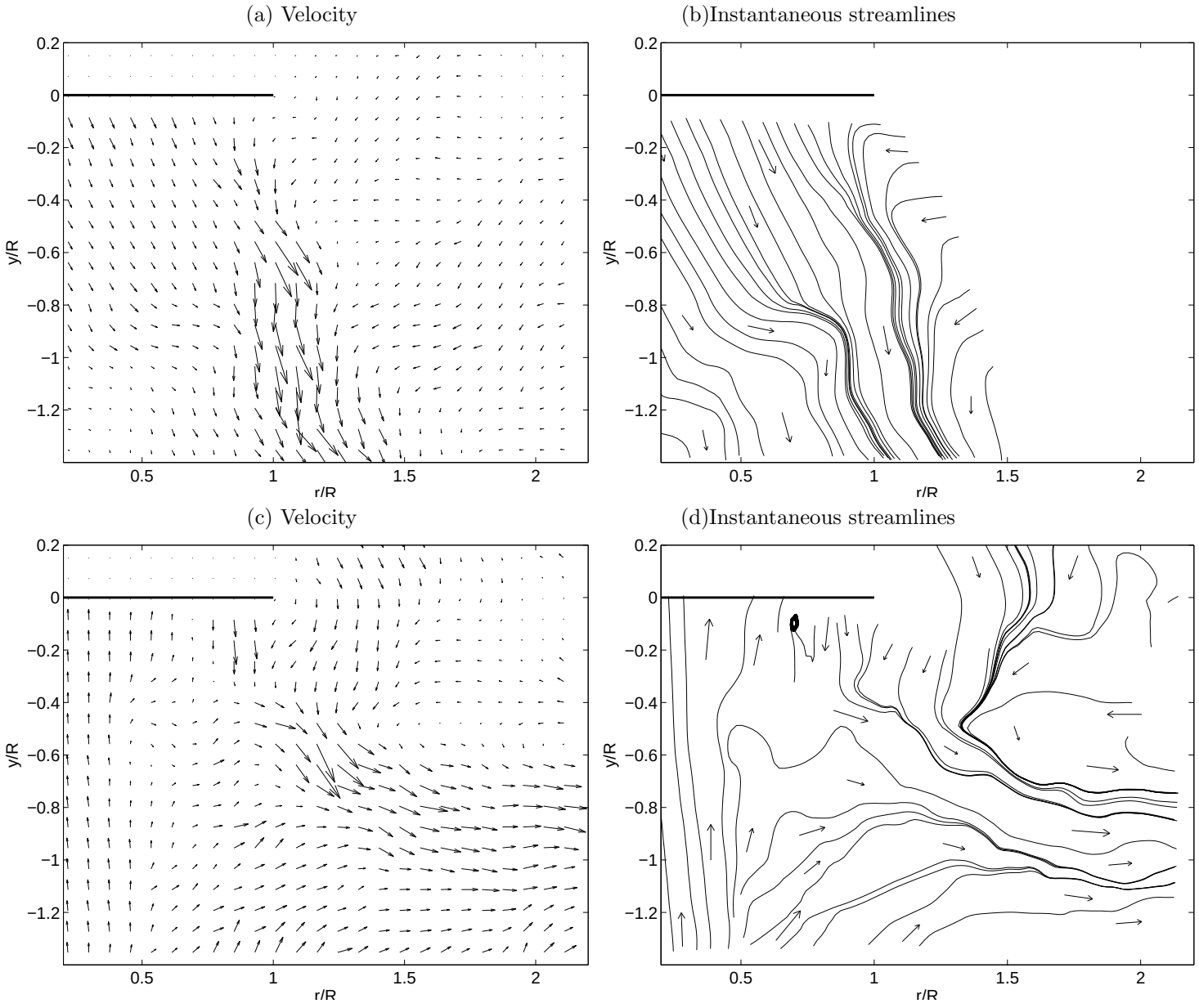

Figure 13: Individual PIV snapshots for annular jet at $\frac{V_d}{V_i} = 0.73$ showing (a), (b) high correlation with hover mean flow (correlation coefficient 0.79) and (c), (d) high correlation with deep VRS mean flow (correlation coefficient 0.9).

(a) Velocity

(b)Instantaneous streamlines

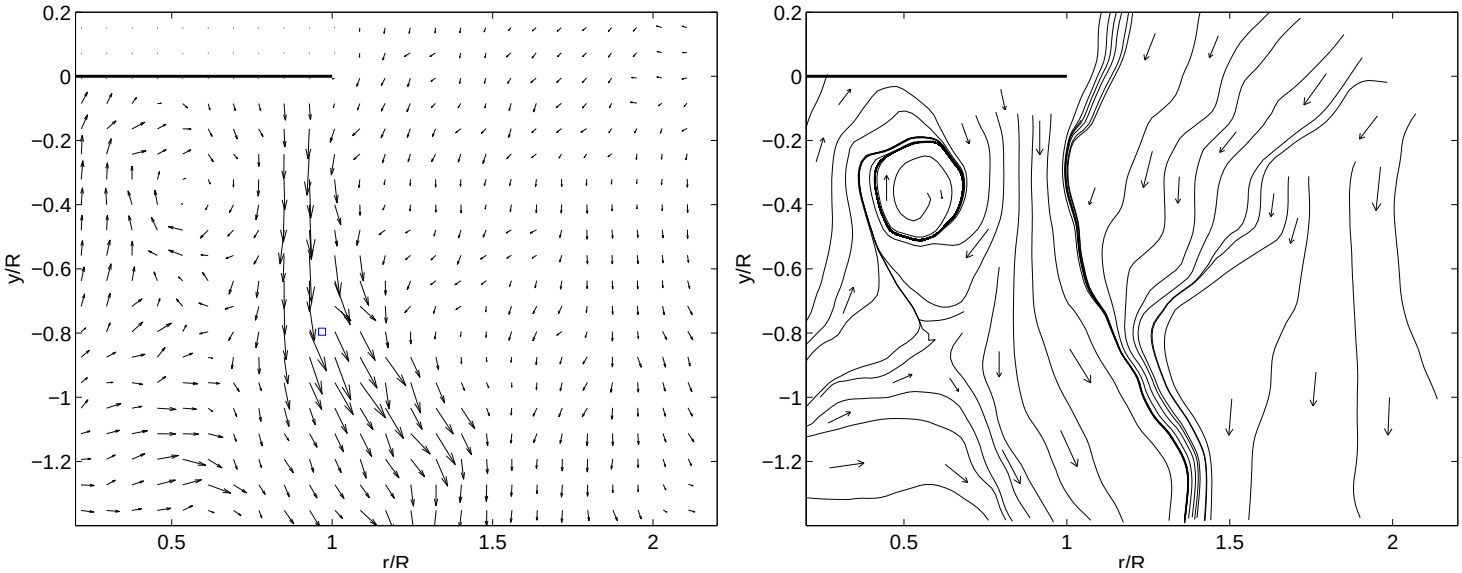

Figure 14: Individual PIV snapshot for annular jet at $\frac{V_j}{V_i} = 0.73$ showing moderate correlation coefficient of 0.55 with both hover and VRS templates.